
Article:
Taylor, D.J., Saxton, H. orcid.org/0000-0001-7433-6154, Halliday, I. et al. (11 more authors) (2024) Evaluation of models of sequestration flow in coronary arteries—physiology versus anatomy? Computers in Biology and Medicine, 173. 108299. ISSN 0010-4825

https://doi.org/10.1016/j.compbiomed.2024.108299

Computers in Biology and Medicine 173 (2024) 108299

Contents lists available at ScienceDirect

Computers in Biology and Medicine

journal homepage: www.elsevier.com/locate/compbiomed

Evaluation of models of sequestration flow in coronary arteries—Physiology versus anatomy?

Daniel J. Taylor [a,c,*], Harry Saxton [e], Ian Halliday [a,c], Tom Newman [b,c], Jeroen Feher [d], Rebecca Gosling [a,b,c], Andrew J. Narracott [a,c], Denise van Kemenade [a,g], Marcel van't Veer [f,g], Pim A.L. Tonino [f,g], Michel Rochette [d], D. Rodney Hose [c], Julian P. Gunn [a,b,c], Paul D. Morris [a,b,c]

[a] Division of Clinical Medicine, School of Medicine and Population Health, University of Sheffield, Sheffield, United Kingdom
[b] Department of Cardiology, Sheffield Teaching Hospitals NHS Foundation Trust, Sheffield, United Kingdom
[c] Insigneo Institute for in Silico Medicine, University of Sheffield, Sheffield, United Kingdom
[d] ANSYS, Villeurbanne, France
[e] Materials & Engineering Research Institute, Sheffield Hallam University, Sheffield, United Kingdom
[f] Department of Cardiology, Catharina Hospital, Eindhoven, Netherlands
[g] Department of Biomedical Engineering, Eindhoven University of Technology, Eindhoven, Netherlands

ARTICLE INFO

Keywords:
Hemodynamics
vFFR
Coronary modelling
Computational fluid dynamics

ABSTRACT

Background: Myocardial ischaemia results from insufficient coronary blood flow. Computed virtual fractional flow reserve (vFFR) allows quantification of proportional flow loss without the need for invasive pressure-wire testing. In the current study, we describe a novel, conductivity model of side branch flow, referred to as 'leak'. This leak model is a function of taper and local pressure, the latter of which may change radically when focal disease is present. This builds upon previous techniques, which either ignore side branch flow, or rely purely on anatomical factors. This study aimed to describe a new, conductivity model of side branch flow and compare this with established anatomical models.

Methods and results: The novel technique was used to quantify vFFR, distal absolute flow (Qd) and microvascular resistance (CMVR) in 325 idealised 1D models of coronary arteries, modelled from invasive clinical data. Outputs were compared to an established anatomical model of flow. The conductivity model correlated and agreed with the reference model for vFFR ($r = 0.895$, $p < 0.0001$; +0.02, 95% CI 0.00 to + 0.22), Qd ($r = 0.959$, $p < 0.0001$; −5.2 mL/min, 95% CI −52.2 to +13.0) and CMVR ($r = 0.624$, $p < 0.0001$; +50 Woods Units, 95% CI −325 to +2549).

Conclusion: Agreement between the two techniques was closest for vFFR, with greater proportional differences seen for Qd and CMVR. The conductivity function assumes vessel taper was optimised for the healthy state and that CMVR was not affected by local disease. The latter may be addressed with further refinement of the technique or inferred from complementary image data. The conductivity technique may represent a refinement of current techniques for modelling coronary side-branch flow. Further work is needed to validate the technique against invasive clinical data.

1. Introduction

Ischaemic heart disease (IHD) is the leading cause of death worldwide. It results, most commonly, from occlusive epicardial stenoses that reduce coronary blood flow. Invasive quantification of proportional flow (Q) obstruction with fractional flow reserve (FFR) is the current gold standard evaluation of epicardial lesion significance, quantifying proportional reduction in coronary Q [1]. Compared with standard angiography, FFR-guided revascularisation improves patient outcomes [2]. However, FFR increases procedural time, cost, and risk of complication [3,4]. Computed coronary physiology, derived from computational fluid dynamics (CFD) simulations, provides an alternative to traditional invasive indices of coronary Q, negating the need for invasive pressure-wire assessment.

Clinical CFD workflows commonly utilise geometries reconstructed from either CT [5] or planar coronary angiography [6]. As the latter may be performed in the cardiac catheterisation laboratory whilst patients lay on the operating table, planar angiography-derived CFD has been proposed as a tool for rapid physiological assessment, informing

* Corresponding author.
E-mail address: daniel.taylor@sheffield.ac.uk (D.J. Taylor).

https://doi.org/10.1016/j.compbiomed.2024.108299
Received 19 November 2023; Received in revised form 8 February 2024; Accepted 12 March 2024
Available online 18 March 2024

clinical decisions in real time [7]. The approach to coronary geometric reconstruction from planar angiography may be subcategorised into truncated tree (TT) [8–14] and single lumen (SL) models [6,15]. In TT models, side branches (typically >1 mm diameter [8,9]) of major bifurcations originating from the vessel of interest are included in geometries. Flow is then partitioned between bifurcation daughter branches by prescribing either flow splitting or a distal boundary resistance (R) according to Murray's law of vascular scaling [16]:

$$Q \propto D^c, \qquad R \propto D^{-c}. \tag{1}$$

Above, D is the diameter of the daughter vessel. Murray's original law predicted a power exponent (c) of 3.0, with subsequent theoretical analyses suggesting a range between 2.0 and 3.0 [16–18]. One issue of TT models is the magnitude of side branches that may be included in reconstructions is limited by the resolution of planar angiography, with vessels less than 1 mm frequently excluded. Moreover, inclusion of multiple bifurcations increases geometry complexity and may therefore prolong reconstruction and simulation time, limiting utility for informing real time clinical decisions.

Unlike TT models, SL models consider only the coronary artery of interest. The lack of side branch inclusion means they neglect side branch Q [6,15]. Recent developments have used Murray's law to infer the diameter, and therefore flow loss, of side branches from the degree of taper of the reconstructed vessel. These techniques distribute side branch flow loss by modelling the reconstructed vessel with a porous wall boundary, prescribing a wall leakage that is a function of the taper. This was first described by Gosling et al. who assumed an even distribution of side branches in the stream-wise direction of the vessel and thus described uniform flow loss along the entire length of the vessel [19]. This 'homogenous' technique was initially validated using a 1D model of coronary flow, in arteries from 80 patients with confirmed coronary artery disease (CAD), where inclusion of side branch losses significantly changed absolute Q, but not virtual FFR (vFFR) [19]. A second 'regional' porous wall method was later developed, in which side branch Q was distributed according to local healthy vessel taper [20]. These SL models of side branch Q, therefore, capture the cumulative effect of all side branches across the length of reconstructed vessel, including those too small to be visualised with planar angiography. They may also allow for faster reconstruction and simulation times, compared with TT models.

A common theme amongst current TT and SL models is that both determine the magnitude of side branch Q purely from local vessel geometry, meaning side-branch Q is unaffected by the local pressure field. For the in-vivo artery, a stenosis would decrease distal pressure, and in turn, likely affect local flow profiles and distal side branch Q. This physics is not represented in current, anatomically based, models of side branch Q. While such approximations may be acceptable for deriving 'virtual' FFR (vFFR) [19,21], the emerging importance of absolute coronary flow (mL/min) [22,23] and wall shear stress [24] demands updated methodology, better able to capture the true *in-vivo* flow phenomena. In this study, we aim to describe a novel physics based, wall conductivity-dependent porous wall method that incorporates the influence of local pressure fields into 1D side branch Q simulation. We also refine the current 1D model of anatomical side branch Q, to account for side branch losses in the treatment of fluid inertia (termed modified anatomical). To determine what is most clinically relevant for modelling side branch Q, we investigate effects of these novel models of flow on vFFR, absolute distal Q (Qd) and coronary microvascular resistance (CMVR) in idealised coronary arteries, adapted from invasive clinical data. Of this analysis, our primary outcome was to compare pre-existing (reference) anatomical and novel conductivity models of flow. Secondary outcomes included comparison of reference and modified anatomical models and an analysis of the effect of varying Murray's flow-diameter exponent.

2. Methods

2.1. Clinical data

Data were collected from adult patients (≥18 years old) undergoing physiological assessment for evaluation of suspected myocardial ischaemia with non-obstructive coronary arteries (INOCA) at the Catharina Hospital, Eindhoven, NL. Absolute flow in mL/min and proximal pressure at the corresponding location were measured using the continuous infusion thermodilution technique and Rayflow™ catheter [23,25]. Patients provided informed consent and data collection was approved by the research ethics board [Medical research Ethics Committees United (MEC-U)]. These patient-specific quantities were used to define the luminal, proximal flow and proximal pressure boundary conditions (BC) for calculations (See Section 2.4.3).

2.2. Vessel segmentation and idealised geometry construction

3D vessel anatomy was reconstructed from two angiographic projections [6], separated by ≥30°. The reconstruction inlet was placed at the location of invasive flow and pressure assessment and the outlet, 4–6 cm distal to this point. All vessels were free of focal epicardial disease, which was confirmed with visual analysis and 3D quantitative coronary angiography (QCA). At least one case of each of the three major epicardial arteries (left anterior descending, left circumflex and right coronary artery) were included, to represent the normal range of coronary anatomy and disease. Radius data were sampled along the centre line of the reconstructed vessel, using 200 points for each centreline, to produce a 1D axi-symmetric model of each vessel. The vessel was characterised by the graph $(x_i, r_i), i \in \{0, 1, 2, ..200\}$, where x was the stream-wise co-ordinate. For $x_i \leq x \leq x_{i+1}$, r_i was assumed to vary linearly, so that the vessel was comprised of segments, each of which was a conical frustum, with its circular faces centred upon the sample points x_i. See Fig. A.6. Filtration was used to ensure that vessel radius was a monotonically decreasing function (Fig. 1). These vessels formed the baseline healthy cases upon which focal stenoses were imposed to generate idealised cases. For a full description of the patient-specific geometries used please Fig. B.7 and Table 1.

2.3. Hemodynamic descriptions

2.3.1. Hemodynamics within a healthy vessel

Fossan et al. first used 1D model models of flow as a basis for quantitative assessment of vFFR. Gosling et al. then adapted this methodology to expose the role of sequestration flow or leak [19,21,26]. To maintain consistency with this prior art, we used a similar 1D model, which is solved numerically. Our three 1D models of vessel flow are all derived in the appendices and are used to compute the flow and pressure as functions of the stream-wise co-ordinate, x. All required the same input data:

1. The artery luminal boundary, in form of $r(x)$ data
2. The patient-specific proximal flow
3. The patient-specific proximal pressure

The models designated reference anatomical and modified anatomical employ anatomical leak. For anatomical models, sequestration flow was determined entirely from the vessel geometry, with pressure a derived quantity. In the conductivity model, the sequestration flow was determined by a known wall conductance function $K(x)$.

All three models rely on boundary (initial) conditions for pressure and flow

$$p(0) = p_0, \quad Q(0) = Q_0 \tag{2}$$

and compute the pressure and flow within a set of vessels which are synthesised from the six geometries and the virtual stenoses. In all

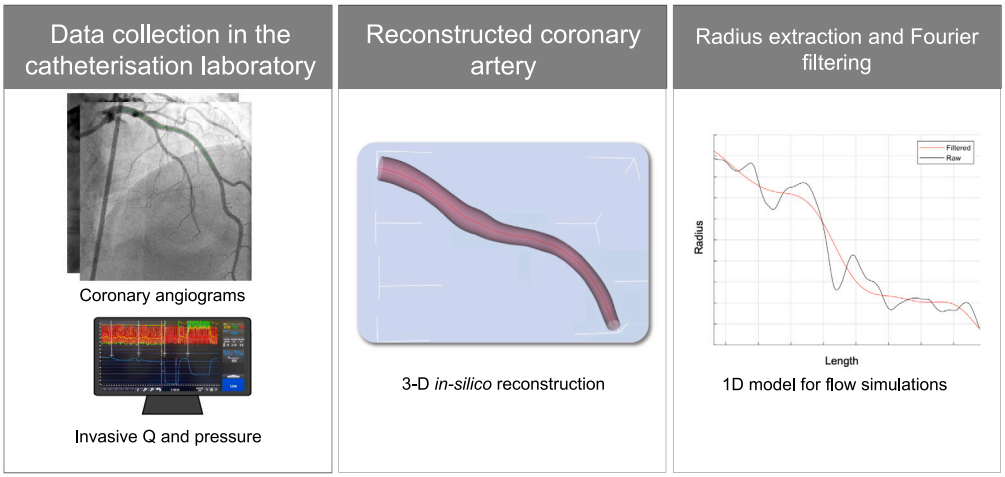

Fig. 1. Schematic of computational workflow from clinical data acquisition (left), through 3D reconstruction (middle) to reduction to 1D and filtration (right).

models the boundary conditions, stenosis and vessel geometry fully determine the distal flow and pressure and therefore an effective CMVR:

$$\text{CMVR} = \frac{P_d}{Q_d} \tag{3}$$

where P_d and Q_d represent the distal pressure and flow respectively.

2.3.2. Reference anatomical model

This model was validated by Gosling et al. on patient data [19]. From the Navier–Stokes equation and a leak-free form of the continuity equation, applied between the ith and (i+1)th segment of vessel (see Fig. A.6), we show in Appendices A.4 and A.5 that

$$p(x_{i+1}) = p(x_i) + \frac{\rho Q_i^2}{2A_i^2} - \frac{\rho Q_{i+1}^2}{2A_{i+1}^2} - 2(\zeta+2)\pi\mu \int_{x_i}^{x_{i+1}} Q(x)A(x)^{-2}dx. \tag{4}$$

Above p_i, Q_i denote the pressure and flow at the inlet of the ith conic frustum segment of the vessel, $\mu = 3.5 \times 10^{-3}$ Pa s is the viscosity of blood, $\rho = 1050$ kg/m^3 and $\zeta = 4.31$ is a dimensionless empirical parameter [19,21,27], obtained from computational fluid dynamics. In the integrand, luminal area $A(x) : x_i \le x \le x_{i+1}$ is obtained straightforwardly, from an assumed linear variation within the segment, of the vessel radius (see Appendix A.2). $Q(x)$ is obtained from the anatomical leak model (see Appendix A.5), in the form $Q(x) = Q_i \left(\frac{\pi r_i(x)^2}{A_i}\right)^{\frac{c}{2}}, 0 \le x \le (x_{i+1} - x_i)$. Flow at the circular faces of each conical frustum segment was assigned as follows:

$$Q_i = Q_0 \left(\frac{A_i}{A_0}\right)^{\frac{c}{2}}. \tag{5}$$

where c is the Murray exponent, inlet (proximal) pressure p_0 and flow Q_0, were measured patient-specific values, which modulate as discussed in Section 2.4.3. The numerical solution (in the absence of a stenotic perturbation) computed pressures and flow at the faces of 200 conical frustra, from Eqs. (4) and (5) respectively.

2.3.3. Modified anatomical model

From the Navier–Stokes and leaky continuity equations, applied to ith conic frustum segment (see Fig. A.6), we use in Appendix A.5 an alternative, decoupled pressure quadrature which takes account of vessel leak in the inertia term

$$p(x_{i+1}) = p(x_i) + \rho\left(\frac{c-1}{c-2}\right)\frac{Q_i^2}{A_i^2} - \rho\left(\frac{c-1}{c-2}\right)\frac{Q_{i+1}^2}{A_{i+1}^2} - \frac{2(\zeta+2)\pi\mu Q_0}{A_1^{\frac{c}{2}}}\int_{x_1}^{x_{i+1}} A^{\frac{c}{2}-2}dx \tag{6}$$

where all constants are defined as above, computation of flow used Eq. (5); inlet (proximal) pressure p_0 and flow Q_0, which were measured patient-specific values.

2.3.4. Conductivity model

This model may be expressed as an initial value problem- a coupled system of non-linear, first-order ordinary differential equations for $p(x)$ and $Q(x)$ together with the boundary conditions (or initial conditions) for $x = 0$ stated above

$$\begin{aligned} \frac{dQ}{dx} &= -\frac{K(x)}{\delta x}p(x) \\ \frac{dp}{dx} &= \frac{\rho}{A^3}\frac{dA}{dx}Q^2 + \frac{2\rho K(x)}{A^2}Qp(x) - \frac{2(\zeta+2)\pi\mu}{A^2}Q \end{aligned} \tag{7}$$

For full derivation see Appendix A.6. The above system was solved using an explicit Runge–Kutta (4,5) algorithm [28]. Given a 'hydraulic conductance' function, $K(x)$, obtained from pressure and flow solutions $p(x), Q(x)$ from the operation of our gold standard reference anatomical model using the following

$$K(x) = \frac{c}{2}\frac{d\log(A)}{dx}\frac{Q(x)}{p(x)}, \tag{8}$$

which was derived in Appendix A.6 from Darcy's law [29], alongside some simple (to state) assumptions. Accordingly, our artery wall conductivity is, by construction, consistent with Murray's law. Crucially, we assumed that $K(x)$ was stationary on timescales characteristic of atherogenesis. A function $K(x)$ was computed for each of the six vessel geometries, which is characteristic of that vessel in health.

2.4. Stenosed model of flow

Only focal, concentric stenoses were considered. The abrupt changes in geometry encountered at stenoses involve significant radial flow, invalidating the assumptions of 1D hydrodynamics. Hence, to facilitate the introduction of the stenoses, a separate sub-model was required for use alongside our models of flow through the un-stenosed vessel part. In 2011 Liang et al. [27] utilised, from previous experimental work [30,31], a relationship between the pressure drop across and flow through a severe constriction applied to the circle of Willis. In the stenosed model of flow, pressure loss is derived from a Bernoulli resistor, with a characteristic equation:

$$\Delta p(Q) = AQ + BQ|Q|, \quad A = \frac{K_v\mu}{A_0 D_0}, \quad B = \frac{K_t\rho}{2A_0^2}\left(\frac{A_0}{A_s} - 1\right). \tag{9}$$

Here, A_0 and A_s are the cross-sectional areas of the healthy and stenotic segments, respectively, D_0 and D_s are the healthy and stenotic vessel

diameters, while K_v and K_t are empirical constants:

$$K_v = \frac{32(0.83L_s + 1.64D_s)}{D_0}\left(\frac{A_0}{A_s}\right)^2, \quad K_t = 1.52.$$

where, L_s is the length of the stenosis and L_0 the length of the parent vessel. All parameters used were the same as in previous literature [27,30]. No leak occurs in the stenosed section of the artery.

2.4.1. Idealised geometry reconstruction

The focal stenosis introduced into the healthy patient specific geometries, further information in Fig. B.7 and Table 1, were artificially parameterised as follows

$$\begin{aligned} L_s &= 3, 5, 7 \text{ mm}, \\ \frac{x_s}{L_0} &= \frac{n}{4}, n \in \{1, 2, 3\}, \\ \frac{A_s}{A_0} &= \frac{m}{20}, m \in \{10, 11, \ldots, 18\}. \end{aligned} \tag{10}$$

where x_s denotes the location of the centre of the stenosis. This set of stenoses were used to 'perturb' healthy vessels. Such configurations were applied to represent the range of epicardial disease within the clinically ambiguous 'grey zone', in which advanced CFD assessment is most clinically useful. In this way, an ensemble of $3 \times 3 \times 9 \times 6 = 486$ virtual patient arteries were synthesised. Simulations were performed primarily using Murray's exponent of $c = \frac{7}{3}$, reflecting the most commonly accepted morphometric scaling law [17]. To investigate the effects of varying this coefficient, Murray's original exponent of 3.0 was also used and compared against results obtained using $\frac{7}{3}$ [16].

2.4.2. Calculation methodology

To determine the pressure and flow in the presence of a stenosis, the perturbed vessel was divided into three sections: from proximal to distal

1. A leaky, unstenosed proximal segment $x < \left(x_s - \frac{L_s}{2}\right)$, was solved utilising one of the models detailed above (reference anatomical, modified anatomical, conductivity). The segment was initialised by a modulated form of the patient-specific aortic signals p_0 and Q_0 (see below), yielding values of $p(x), Q(x) : x \leq \left(x_s - \frac{L_s}{2}\right)$.
2. A non-leaky stenosed segment $x : \left(x_s - \frac{L_s}{2}\right) \leq x \leq \left(x_s + \frac{L_s}{2}\right)$, solved using Eq. (9) and $Q\left(x_s - \frac{L_s}{2}\right)$ (from step (1)), yielding $\Delta p\left(Q(x_s - \frac{L_s}{2})\right)$.
3. A leaky healthy distal section $x > \left(x_s + \frac{L_s}{2}\right)$, again solved using the model in (1) above, bounded by a pressure $p\left(x_s + \frac{L_s}{2}\right) + \Delta p\left(Q(x_s - \frac{L_s}{2})\right)$ (from steps (1) and (2) above) and a flow $Q\left(x_s - \frac{L_s}{2}\right)$, from (1).

For non-stenosed cases, patient-specific invasively measured Rayflow™ absolute flow measurements defined the inlet flow boundary condition and the healthy vessel's conductivity function, $K(x)$. Introducing a stenosis increases the resistance of the vessel, reducing its inlet flow (for a given proximal pressure). Accordingly, the measured inlet flow used to inform the proximal calculation in step (1) above should be modulated for each stenosis, as described in Section 2.4.3.

2.4.3. Inlet boundary condition modulation

For all cases, invasive measured proximal pressure was used to inform the inlet pressure boundary condition, p_0. However, since the invasive inlet flow result is invalidated when stenotic perturbations are introduced, particularly for the more severe stenoses, Q_0 should be personalised, according to the vessel vFFR

$$Q_0 \rightarrow \text{vFFR} \times Q_0, \quad \text{vFFR} \equiv \frac{p_d}{p_0}. \tag{11}$$

Above, p_d denotes the pressure distal to the stenosis. Let Q_0' denote the personalised value of Q_0, which may be determined in a way which is consistent with the assumptions of FFR and our most validated reference anatomical model of flow [19,21,32]. Assuming the pressure drop across the stenosis dominates proximal pressure losses, Eq. (9) gives $p_d \approx p_0 - \Delta p(Q)$, hence

$$\text{vFFR} = \left(\frac{p_0 - \Delta p(Q)}{p_0}\right) = 1 - \frac{(AQ + BQ|Q|)}{p_0}.$$

Here, Q is the stenosis inlet flow $Q = Q_0'\left(\frac{A(x_s)}{A(0)}\right)^{p/2} \equiv k_0 Q_0'$. Hence, from Eqs. (11)

$$vFFR = \frac{Q_0'}{Q_0} = 1 - \frac{\left(Ak_0Q_0' + Bk_0^2Q_0'|Q_0'|\right)}{p_0}, \quad k_0 = Q_0\left(\frac{A(x_s)}{A(0)}\right)^{p/2} \tag{12}$$

Assuming $Q_0' > 0$, the above yields a quadratic for our personalised inlet flow, Q_0', with only one positive solution

$$Q_0' = \frac{-\left(Ak_0Q_0 + p_0\right) \pm \sqrt{\left(Ak_0Q_0 + p_0\right)^2 + 4Bk_0^2Q_0^2p_0}}{2Bk_0^2Q_0} \tag{13}$$

The corresponding personalised vFFR may be obtained from vFFR= $\frac{Q_0'}{Q_0}$. Please see Fig. 2 for a schematic of the analysis protocol.

2.5. Statistical analysis

Categorical variables are presented as frequency (percentage) and were compared using Chi-square and logistic regression as appropriate. The Shapiro–Wilk test was used to assess the spread of data. Normally distributed continuous variables are presented as mean (± standard deviation), while skewed data are presented as median [inter-quartile range]. For parametric data, mean values of haemodynamic parameters were compared using an unpaired t-test for two independent samples and a one-way ANOVA to compare three or more samples. For non-parametric data, the Mann–Whitney U test was used to compare two independent samples and the Kruskal Wallis test to compare three or more samples.

Correlation was quantified using Pearson's correlation coefficient (r). Agreement between techniques was quantified using two statistical techniques: Passing and Bablok regression and Bland Altman plots. Passing and Bablok regression was used as this is a nonparametric technique, not sensitive to outliers and therefore well suited to our non-normally distributed data. Regression results are presented as a scatter diagram and regression line bounded by 95% confidence limits shaded in grey. The c and m coefficients represent constant and proportional differences between measurement techniques respectively. Bland Altman plots display the mean bias between techniques and 95% limits of agreement. A statistical threshold of $p \leq 0.05$ was considered significant and all statistical tests were two-tailed.

3. Results

3.1. Patient characteristics and invasive results

Six coronary arteries, taken from five different patients were included. One patient (20%) was male, mean age was 50 (±8) years and mean BMI was 26 (±4). The six arteries comprised four left anterior descending artery's (LAD's), one left circumflex (LCx) and one right coronary artery (RCA). The mean invasively measured hyperaemic flow was 276 (±42) mL/min, while vessel percentage stenosis, as assessed by an experienced interventional cardiologist in two angiographic projections, was ≤5% for all cases examined see (Table 1)

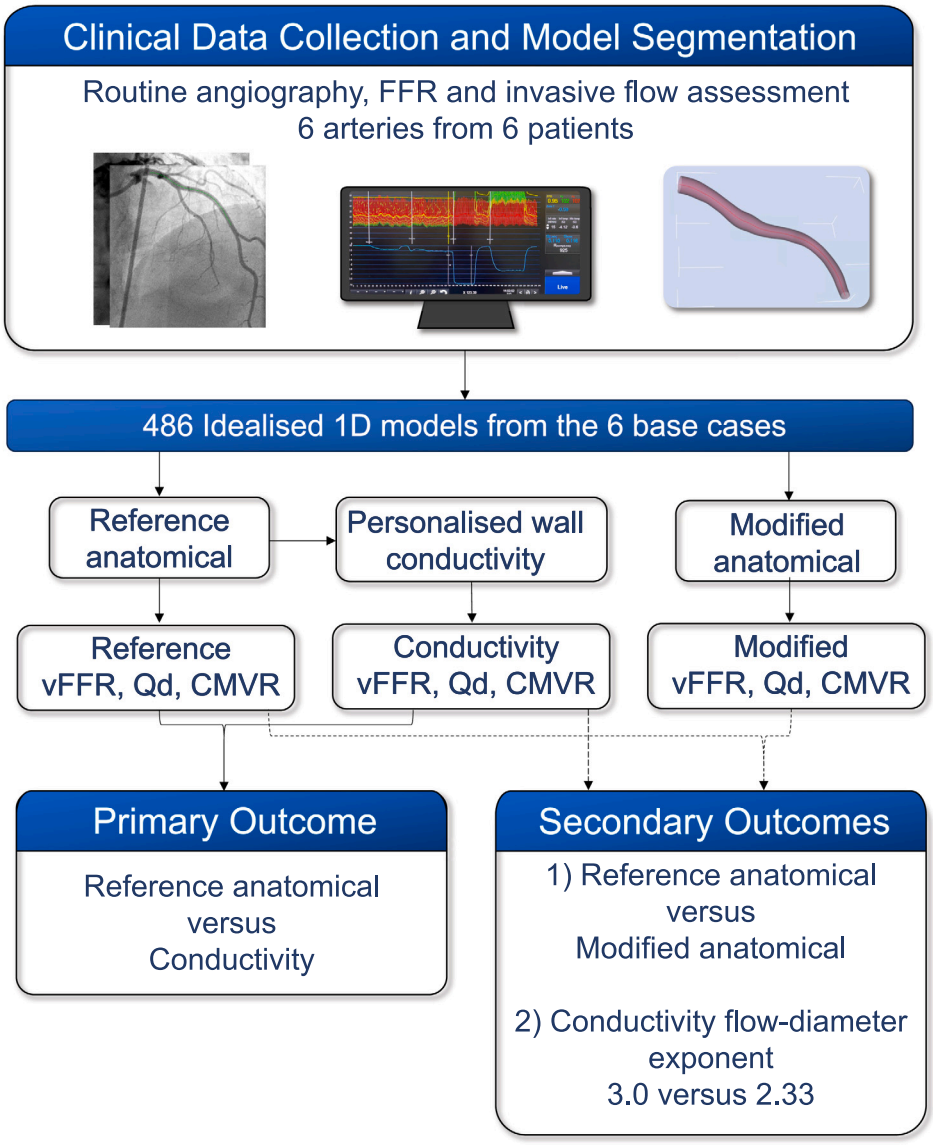

Fig. 2. A schematic of the workflow: Arteries were reconstructed in 3D using angiograms and epipolar geometry. The 3D reconstruction was reduced to 1D by extracting centre-line distance x, and radius $r(x)$. The result was then down-sampled onto a regular 1D mesh with 200 points. These data were then low-pass filtered, by truncating a Fourier series decomposition, to remove small wavelength fluctuations in which $\frac{dr}{dx} > 0$. These 1D geometries were then subject to various parameterisation and inlet flow modulation to create synthetically stenosed arteries which are passed to the models under investigation.

Table 1
Summary of vessel characteristics used to define the healthy arteries used in this study. The vessels summarised here, once filtered, are regarded as healthy and are 'perturbed' with stenosed section, as described in Section 2.4.

Case	Vessel	Q_0 (mL/min)	p_0 (mmHg)	Visual stenosis	Inlet ϕ (mm)	Outlet ϕ (mm)	Length (mm)
1	LCx	332	113	5%	4.21	3.03	44.4
2	RCA	242	102	0%	3.45	3.10	55.9
3	LAD	278	90	0%	2.87	1.19	60.0
4	LAD	333	83	0%	2.52	1.44	43.8
5	LAD	234	81	0%	2.98	1.37	40.9
6	LAD	239	100	0%	3.42	2.22	47.6

3.2. Case exclusions

For the conductivity model, out of 486 attempts there were deemed to be 325 (66.9%) successful simulations. In all cases, exclusions were attributed to failure of the algorithm used to modulate inlet flow and not instability in the ODE solver. This resulted from excessive imbalance between disease burden and inlet flow in the non-diseased state. Accordingly, simulation failure was associated with increasing percentage stenosis (chi-square 43,69, $p < 0.0001$). When using a Murray's exponent of 3.0, 307 (63.2%) attempted simulations were successful, which did not significantly differ when using an exponent of 7/3 (chi square 1.64, $p = 0.201$).

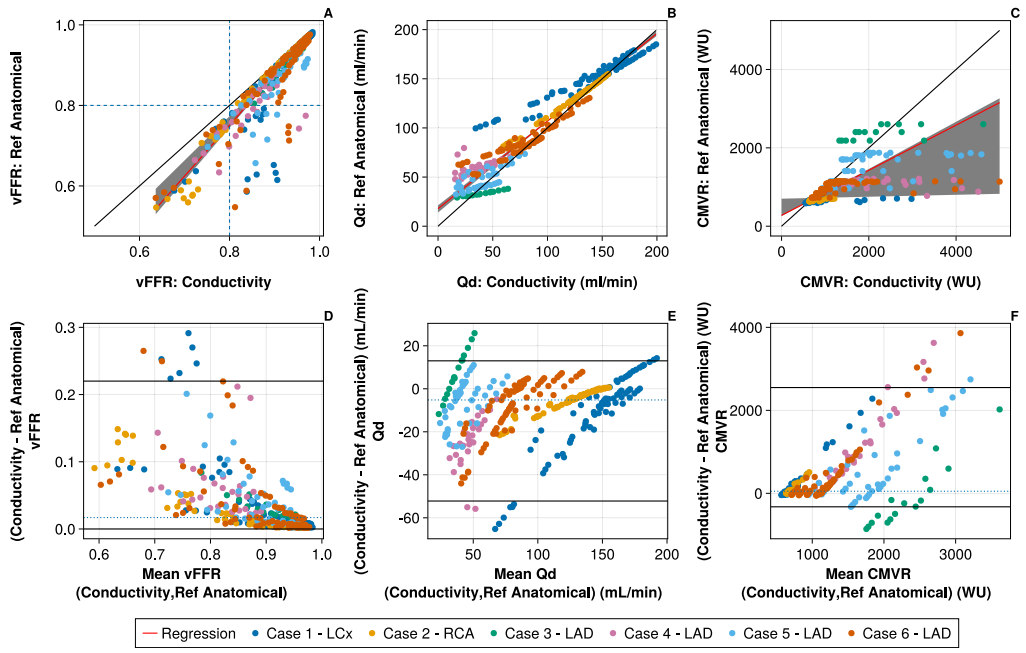

Fig. 3. Comparison of conductivity and reference anatomical model operation on equivalent synthetic stenoses, across all six arteries. Arteries' data are colour coded (see figure legend). Panels A, B and C depict Passing and Bablok regression for vFFR, distal flow (Qd) and coronary micro-vascular resistance (CMVR) respectively. The identity line is given in black with the regression line in red with corresponding confidence limits depicted by the grey shaded regions. Panels D, E and F show Bland Altman plots with median overall bias (dashed blue line) and 95% CI (solid black line).

3.3. Conductive vs. Reference anatomical

For the conductivity and reference anatomical functions, as seen in Fig. 3, paired data was available for 325 simulations. From this, median vFFR was 0.92 [0.86–0.96] using the conductivity function and 0.90 [0.81–0.95] using the reference anatomical function. Correlation between the two functions was statistically significant (r = 0.895, $p < 0.0001$). Passing and Bablok regression identified constant and proportional differences between techniques (m = 1.27, 95% CI 1.10 to 1.31; c = −0.26, 95% −0.11 to −0.30], in Fig. 3A and D. Relative to the reference anatomical function, the conductivity function overestimated vFFR by +0.02 (95% CI 0.00 to +0.22). Agreement was inversely correlated with vFFR (r = −0.471, $p < 0.0001$). Intended management (i.e., vFFR ≤ 0.80) between conductivity and reference anatomical changed in 38 (11.7%) cases, of which all reclassified as physiologically non-significant with the conductivity function.

As seen in Fig. 3B and E, Median Qd was 90.4 [50.1–135.9 mL/min] using the conductivity function and 102.9 [63.8–138.8 mL/min] using the reference anatomical function. Correlation between the two functions was significant (r = 0.959, $p < 0.0001$). Passing and Bablok regression identified constant and proportional differences between techniques (m = 0.89, 95% CI 0.86 to 0.93; c = 17.8, 95% 13.9 to 21.3). Relative to the reference anatomical function, the conductivity function underestimated Qd by −5.2 (95% CI −52.2 to +13.0 mL/min). Correlation between Qd agreement with vFFR was significant (r = −0.526, p < 0.0001)(indicating better agreement between conductivity and reference Anatomical Qd in cases with less severe stenoses).

In Fig. 3C and F, Median CMVR was 959 [722–1604 WU] using the conductivity function and 730 [698–1142 WU] using the reference anatomical function. Correlation between the two functions was significant (r = 0.624, $p < 0.0001$). Passing and Bablok regression identified constant and proportional differences between techniques (m = 0.58, 95% CI 0.03 to 0.60; c = 277, 95% CI 258 to 702). Relative to the reference anatomical function, the conductivity function overestimated CMVR by +50 (95% confidence interval −325 to +2549 WU).

3.4. Modified anatomical vs. Reference anatomical

For the modified and reference anatomical models, as seen in Fig. 4, paired data was available for 438 simulations. From this, median vFFR was 0.87 [0.75–0.94] using the modified anatomical function and 0.86 [0.74–0.93] using the reference anatomical function. In Fig. 4A and D, correlation between the two functions was significant (r = 0.997, $p < 0.0001$), as expected. Passing and Bablok regression identified constant, but not proportional differences between techniques (m = 1.005, 95% CI 0.9997 to 1.011; c = −0.01, 95% CI −0.0056 to −0.0155]. Relative to the reference anatomical function, the modified anatomical function overestimated vFFR by +0.01 (95% confidence interval 0.00 to +0.04). Intended management (i.e., vFFR ≤ 0.80) between modified and reference anatomical changed in ten (2.3%) cases, of which all reclassified as physiologically non-significant with the modified anatomical function.

Fig. 4B and E display the median Qd was 78.6 [39.9–133.7 mL/min] using the conductivity function and 78.6 [39.9–133.7 mL/min] using the reference anatomical function. Correlation between the two functions was significant (r = 1, $p < 0.0001$). Passing and Bablok regression did not identify constant or proportional differences between techniques (m = 1.00, 95% CI 1.00 to 1.00; c = 0.00, 95% CI 0.00 to 0.00. There was zero overall bias between modified and reference anatomical functions (95% CI 0.0 to 0.0 mL/min).

Median CMVR, shown in Fig. 4C and F was 1084 [705–1819 WU] using the modified anatomical function and 1057 [702–1802 WU] using the reference anatomical function. Correlation between the two functions was significant (r = 0.999, $p < 0.0001$). Passing and Bablok regression identified proportional, but not constant, differences between techniques (m = 0.975, 95% CI 0.973 to 0.998; c = 19.0, 95% CI −5.0 to 16.0). Relative to the reference anatomical function, the modified anatomical function overestimated CMVR by +8 (95% confidence interval +1 to +84 WU).

3.5. Effect of Murray exponent

To provide insight into the significance of Murray's exponent for quantifying virtual physiology, vFFR (Fig. 5A and D), Qd (Fig. 5B and

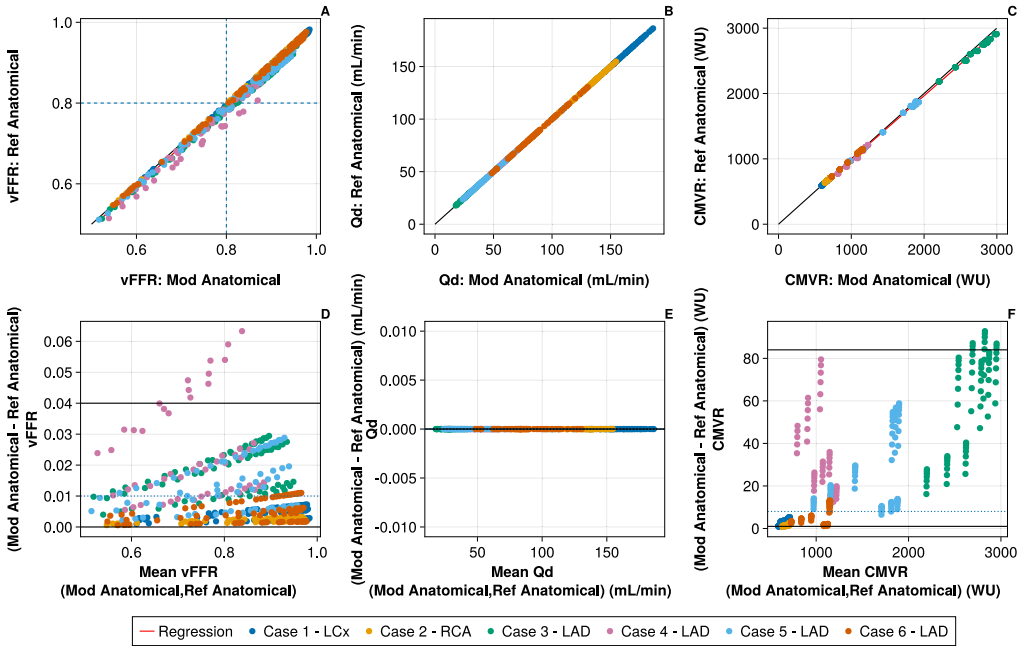

Fig. 4. Comparison of the modified and reference anatomical model operation on equivalent synthetic stenoses, across all six arteries. Panels A, B and C depict Passing and Bablok regression for vFFR, distal flow (Qd) and coronary micro-vascular resistance (CMVR) respectively. The identity line is given in black with the regression line in red with corresponding confidence limits depicted by the grey shaded regions. Panels D, E and F show Bland Altman plots with median overall bias (dashed blue line) and 95% CI (solid black line).

E) and CMVR (Fig. 5C and F) were computed using exponents of 7/3 and 3.0 with the conductivity model, results are presented in Fig. 5. Paired data were available for 303 simulations. From this, median vFFR was 0.92 [0.87–0.96] using an exponent of 7/3 and 0.94 [0.89–0.96] using an exponent of 3.0. Correlation between these results was significant (r = 0.994, $p < 0.0001$). Passing and Bablok regression did not identify constant or proportional differences between exponent used (m = 0.90, 95% CI 0.89 to 1.14; c = 0.107, 95% CI - 0.118 to 0.111). Relative to using an exponent of 7/3, using Murray's exponent of 3.0 overestimated vFFR by +0.01 (95% confidence interval 0.00 to +0.04).

Median Qd was 96.5 [57.4–136.6 mL/min] when using an exponent of 7/3 and 84.5 [46.0–121.8 mL/min] when using an exponent of 3.0. Correlation between exponents of 7/3 and 3.0 with the conductivity function was significant (r = 0.993, $p < 0.0001$). Passing and Bablok regression identified constant and proportional differences between exponent used (m = 0.940, 95% CI 0.927 to 0.974; c = −8.87, 95% CI −11.37 to −7.81). Relative to using an exponent of 7/3, using Murray's exponent of 3.0 underestimated Qd by −13.3 (95% confidence interval −27.5 to −6.2 mL/min).

Median CMVR was 893 [719–1412 WU] when using an exponent of 7/3 and 1100 [801–1845 WU] when using an exponent of 3.0. Correlation between using exponents of 7/3 and 3.0 with the conductivity function was significant (r = 0.970, $p < 0.0001$). Passing and Bablok regression identified constant and proportional differences between exponent used (m = 1.522, 95% CI 1.496 to 1.589; c = −280, −339 to −254). Relative to using an exponent of 7/3, using Murray's exponent of 3.0 overestimated CMVR by +195 (95% confidence interval +46 to +1821 WU).

4. Discussion

We have described a novel, wall conductivity-dependent porous wall method that is responsive to both local anatomy and stenosis-induced localised pressure perturbations in its distribution of coronary side branch flow. In-vivo validation of such a technique is challenging as no invasive method to measure and regionalise Q throughout epicardial coronary arteries exists. Therefore, our analysis compared the novel technique with established computational models of coronary physiology that are sensitive only to local anatomy. Specifically, the technique was successfully used to quantify vFFR, Qd and CMVR in 325 idealised 1D models of coronary arteries, adapted from invasive clinical data. The new conductivity function correlated with the established reference anatomical function for vFFR, Qd, and CMVR, with biases of +0.02, −5 mL/min and +50 WU respectively. Agreement between techniques was strongest for vFFR and weaker for Q and CMVR. This is reassuring; prior 1D models of vFFR have strong agreement with invasive results, whereas models of absolute Q and CMVR are likely to display larger variation versus invasive surrogates. The novel technique may therefore represent a refinement of current techniques for simulating side branch flow, whilst still preserving the known diagnostic accuracy for vFFR.

4.1. Current techniques for quantifying translesional physiology

The superiority of translesional pressure indices over standard coronary angiography is well established [33,34]. However, the added time, cost and risk of procedural complication of invasive FFR assessment frequently limits uptake in routine clinical practice [35]. The past decade has seen advancements in modalities for computing vFFR both outside and inside the cardiac catheterisation laboratory. The first vFFR techniques invoked a SL model that neglected side branch flow [6,21]. Newer SL techniques quantified side branch flow from vessel taper [19] and can now regionalise this to the location of bifurcations [20]. There has also been an increase in the use of machine learning techniques to calculate vFFR [32]. Numerous CFD workflows utilising TT models to compute vFFR have also been described. These reconstruct geometries from both CT [5] and planar angiography [8–14] and have a range of clinical uses from pre-procedural planning to informing real-time decision making within the cardiac catheterisation laboratory. Despite these differences, all current vFFR techniques that incorporate side-branch losses invoke an anatomical approach that is not sensitive to local pressure perturbations within coronary arteries.

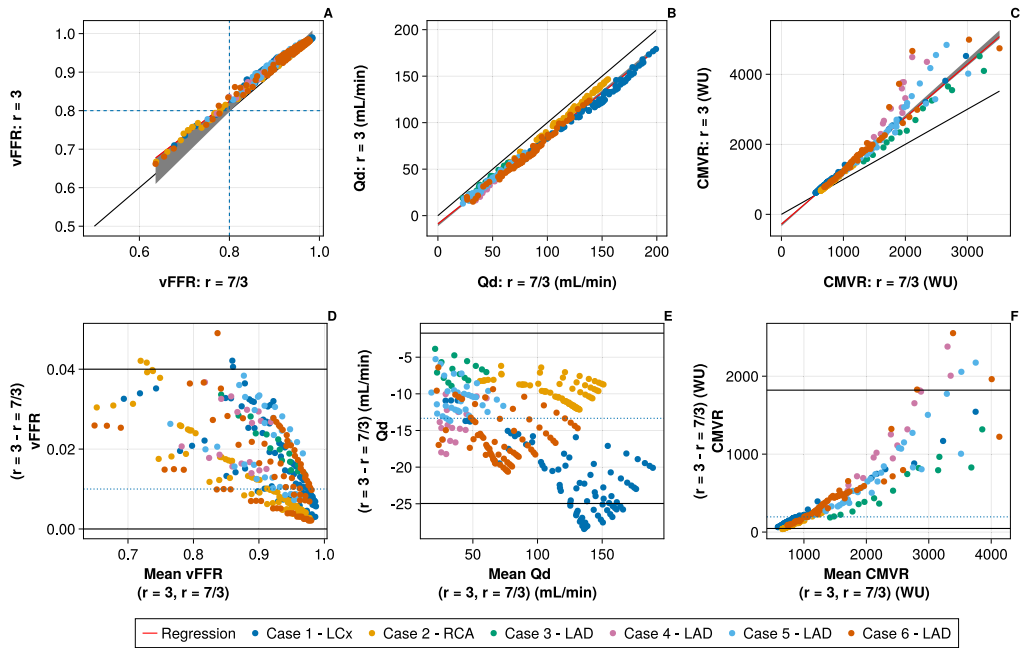

Fig. 5. Comparison of Murray's exponents 7/3 and 3.0 computed using the operation of the conductivity model. Panels A, B and C depict Passing and Bablok regression for vFFR, distal flow (Qd) and coronary micro-vascular resistance (CMVR) respectively. The identity line is given in black with the regression line in red with corresponding confidence limits depicted by the grey shaded regions. Panels D, E and F show Bland Altman plots with median overall bias (dashed blue line) and 95% CI (solid black line).

4.2. Current techniques for quantifying 'complete' coronary physiology

Despite the utility of translesional pressure indices, they may only quantify percentage reduction in coronary flow and give no assessment of microvasculature. As a subject of ongoing research [22], the importance of these limitations is emerging; both European and American guidelines now recommend assessment of CMVR in supporting a diagnosis of coronary microvascular disease [36,37]. However, while assessment of the microvasculature may be achieved with proxy measures of absolute coronary flow such as Doppler or bolus thermodilution, agreement between these techniques is sub-optimal even in expert hands (R^2 = 0.19; p < 0.0001) [38]. Alternative techniques for quantifying absolute CMVR alongside absolute coronary flow (mL/min) and coronary flow reserve (CFR) are now available. The continuous infusion Rayflow™ catheter [23,25] is an invasive technique that is currently used clinically in a small number of tertiary centres. A computational alternative exists [15], which has been previously used to demonstrate sex differences in CMVR [39]. This uses full 3D-CFD simulations and may regionalise absolute flow throughout the coronary artery by invoking an anatomically-informed side-branch leakage function, similar to the reference anatomical approach [20].

4.3. Comparison of conductivity and reference anatomical functions

In the present study, we quantified vFFR, Qd and CMVR, comparing this with an established 1D model of coronary flow. The conductivity function overestimated vFFR by +0.02 (95% CI 0.00 to +0.22), with lower agreement observed at lower vFFR values. This close agreement is reassuring; the reference anatomical approach has itself been shown to have close agreement with invasive FFR (mean bias +0.07, 95% CI −0.20 to +0.29) [19], suggesting minimal additional bias may exist between invasive FFR and vFFR calculated with the conductivity function. Relative to the reference anatomical function, overall diagnostic accuracy (ability to discriminate FFR ≤ 0.80) of the conductivity function was 88.3%, with all discordant cases false negatives (n = 38). This result may be explained through consideration of the physics underpinning the conductivity function:

1. In cases with equivocal or significant stenoses (FFR < 0.85), there is a significant reduction in inlet flow.
2. As the pressure field proximal to the stenosis is relatively unperturbed, the conductivity function leak over this area will not significantly change relative to the unstenosed case. This conservation of absolute proximal leak can result in a lower absolute flow reaching the stenosed section.
3. As leak in the reference anatomical case is dependent only on local vessel taper, a lower inlet flow results in lower leak proximal to the stenosis. This results in a relatively higher flow reaching the stenosed section.
4. The lower flow reaching the stenosis (which approximates a Bernoulli resistor) for the conductivity function results in a lower pressure drop across the stenosis.
5. As pressure drop across the stenosis is the major contributor to vFFR, this results in higher vFFR values with the conductivity, function relative to the reference anatomical technique.

Nevertheless, as sensitivity of the reference anatomical function relative to vFFR is 46% (i.e., the number of hemodynamically significant cases is underestimated), this suggests sensitivity of the conductivity function may also be low when compared with invasive FFR. This difference between conductivity and reference anatomical models versus invasive FFR suggests a systematic error, likely introduced at the stenosed model of flow, which is represented as Bernoulli resistor. This feature of the conductivity model is unique in that it is defined purely by empirically derived parameters and not patient-specific values [27]. As these empirical values were derived from analysis of vessels within the cerebrovasculature, in which compliance is more influential, it is possible they do not best represent those which characterise a stenosed coronary artery. If so, it is likely new parameters, more specific to diseased epicardial coronary arteries will yield better agreement with invasive results.

The conductivity function led to an underestimation of Qd by −5.2 (95% CI −52.2 to +13.0 mL/min), with greater discordance between conductivity and reference anatomical models observed in cases with more severe stenoses. Again, the lower distal flows observed with the reference anatomical function are likely to result from the comparatively smaller vFFR values, as inlet flow is identical for both functions,

this dictates greater side branch losses in order to effect the larger proportional difference between inlet and outlet flow. With no prior validation of Qd results derived using the reference anatomical function versus other quantification techniques, it is difficult to comment on which technique may provide more accurate results. The lower correlation and agreement for CMVR is to be expected; the result is derived from both vFFR and Qd, which themselves are subject to variation between conductivity and reference anatomical functions.

4.4. Comparison of the modified and reference anatomical functions

The agreement between modified and reference anatomical functions was closer for vFFR and CMVR and matched exactly for Qd. Subtle differences in vFFR, and therefore CMVR, may be attributed to differential handling of the inertia terms between the two models. Specifically, the flow-diameter (Murray) scaling exponent exerts greater influence on the modified anatomical function, resulting in differences between Eqs. (2) and (4). While agreement between the two anatomical functions was closer than observed with the conductivity function, management still changed in ten (2%) cases. Of these cases, all were reclassified as haemodynamically significant, according to the modified anatomical function. Given vFFR is the output of these mathematical models with the most immediate and widespread applicability, identification of a further 2% of patients who may benefit from treatment could represent a further, clinically significant refinement of the technique. Contrastingly to vFFR and CMVR, Qd matched exactly between the two anatomical functions. This is because flow was derived from a surrogate continuity equation, which gives flow solely in terms of the vessel geometry and Murray's exponent (see Eq. (A.7)). As neither of these input parameters differed between the two anatomical functions, perfect agreement was expected. These differences in agreement between the two models, therefore, represent an element of decoupling between pressure and flow calculation in the mathematical models. Consequently, subtle variations in methodology, such as our differential handling of inertia terms, may produce results in which the translesional pressure ratio is not exactly equivalent to the proportional reduction in flow:

$$\frac{Qd}{Qo} \approx \frac{Pd}{Pa}$$

While an assumption of equivalence is made in the assessment of invasive FFR, this does not hold strictly true for the computational model.

4.5. Effect of Murray's exponent

Findings for the effect of Murray's law are twofold. Firstly, the effect of varying the exponent between 7/3 and 3.0 on conductivity-derived vFFR was modest, resulting in discordant classification of clinical significance in only eight (2.6%) cases. This result is in agreement with Gosling et al. who suggested Murray's exponent and the inclusion of side branch flow had minimal impact on vFFR [19]. Secondly, in our derivation of the modified anatomical function, we described a new handling of inertia terms that was sensitive to the Murray flow-diameter scaling exponent. The effect of this inclusion was comparable to that observed when varying Murray's exponent between 7/3 and 3.0.

The impact of varying Murray's exponent on Qd and CMVR was more pronounced: a Murray's exponent of 7/3 resulted in universally higher Qd, an effect that was more profound with increasing flow rates. This had knock-on effects for CMVR, which was consistently lower when derived with an exponent of 7/3. These results, therefore, suggest that the importance of Murray's exponent is more significant when computing 'complete' coronary physiology.

4.6. Limitations

Accuracy of the technique is dependent upon faithful reconstruction of patient anatomy, assumptions about imposed boundary conditions and necessitates the reconstruction inlet and outlet are placed in sections of healthy vessel. A disproportionate number of LAD base cases were included, but this is not abnormal of computational studies. Failure rate of the conductivity function was higher than both anatomical functions. This was particularly true for more stenosed and tapered cases and may reduce ability of the technique to be deployed across the broad range of epicardial vessels and stenoses that may be encountered in routine clinical practice. However, with further work, the failure rate of simulations could be reduced. The conductivity function assumes approximately equal distribution of disease in the side branches proximal and distal to a stenosis and effects of vascular remodelling are negligible compared to the timescale of atherogenesis. Several theoretical derivations [16,17] and in-vivo measurements [40–42] of Murray's exponent exist for epicardial coronary arteries, with no current consensus value. A more robust method of modulating the inlet flow should clearly encompass a model of adaptating CMVR, in response to reduced perfusion, which is reserved for future work. The patient cohort who may benefit from virtual coronary physiology and treatment thresholds are uncertain and subject to ongoing research [22,43].

4.7. Future work

As the conductivity function was only directly compared with prior computational techniques, a validation study against invasive clinical data is warranted and already in progress. However, the use of invasive imaging and corresponding physiological data retained as much clinical relevance as possible for an *in-silico* dataset. Validation studies of Qd and CMVR are complicated by the relative lack of invasive clinical measurement tools and absence of any technique for regionalising flow along the coronary artery. Future validation studies will need to carefully address this issue. In addition to validation studies, an extensive global sensitivity analysis is needed to understand inherent uncertainties within the model [44,45]. This would improve understanding of the effects of manipulating input parameters and therefore facilitate model development.

5. Conclusion

The accuracy of vFFR and other virtually-derived indices of coronary flow are dependent upon the precision with which *in-vivo* flow can be reproduced. In this study, we devised and evaluated a novel conductivity function, in which coronary side branch losses are sensitive to local perturbations in pressure. The technique was deployed in 325 idealised coronary geometries, adapted from invasive clinical data. Agreement of vFFR with an established 1D model of coronary flow was strong, with greater differences observed in more stenosed arteries. Further validation work is required, but this technique may represent a refinement in our ability to model local blood flow dynamics while preserving diagnostic accuracy.

Funding

PDM was funded by the Wellcome Trust [214567/Z/18/Z]. For the purpose of Open Access, the author has applied a CC BY public copyright licence to any Author Accepted Manuscript version arising from this submission. His independent research was carried out at the NationalInstitute for Health and Care Research (NIHR) Sheffield BiomedicalResearch Centre (BRC). The views expressed are those of the author(s)and not necessarily those of the NIHR or the Department of Health andSocial Care.

CRediT authorship contribution statement

Daniel J. Taylor: Writing – original draft, Visualization, Methodology, Investigation, Formal analysis, Data curation, Conceptualization. **Harry Saxton:** Writing – original draft, Validation, Software, Methodology, Investigation, Formal analysis. **Ian Halliday:** Writing – original draft, Supervision, Software, Methodology, Investigation, Formal analysis, Conceptualization. **Tom Newman:** Writing – review & editing, Software. **Jeroen Feher:** Writing – review & editing, Software. **Rebecca Gosling:** Writing – review & editing, Software. **Andrew J. Narracott:** Writing – review & editing, Visualization, Software. **Denise van Kemenade:** Writing – review & editing, Conceptualization. **Marcel van't Veer:** Writing – review & editing, Data curation. **Pim A.L. Tonino:** Writing – review & editing, Data curation. **Michel Rochette:** Writing – review & editing, Software. **D. Rodney Hose:** Writing – review & editing, Software, Formal analysis. **Julian P. Gunn:** Writing – review & editing, Supervision. **Paul D. Morris:** Writing – review & editing, Supervision.

Declaration of competing interest

The authors declare that the research was conducted in the absence of any commercial or financial relationships that could be construed as a potential conflict of interest. This independent research was carried out at the National Institute for Health and Care Research (NIHR) Sheffield Biomedical Research Centre (BRC). The views expressed are those of the author(s) and not necessarily those of the NIHR or the Department of Health and Social Care.

Appendix A. Derivation of models

We will advance three steady-state descriptions of artery flow based upon a 1D description. All three will rely upon an appropriate description of the geometry of the luminal boundary. Our three cases are distinguished by the way in which they account for a sequestration flux.

A.1. Formulation of artery flow in 1D

The 1D formulation of artery flow involves integrating the incompressible Navier–Stokes and continuity equations over an arterial section under the assumption

$$\frac{v_r(r,x)}{v_z(r,x)} \simeq \frac{R}{L}$$

with R and L the stream-wise, x and transverse r, co-ordinate length-scales, respectively. In general, pressure $p(x,t)$, flow $Q(x,t)$ and artery cross-section $A(x,t)$ are all dependant upon time, t and stream-wise co-ordinate x. With these variables, the equations of mass and the momentum conservation may be written [46]

$$\begin{aligned} \frac{\partial Q}{\partial x} &= -\frac{\partial A}{\partial t} \\ \frac{\partial Q}{\partial t} + \frac{\partial}{\partial x}\left(\frac{Q^2}{A}\right) &= -\frac{A}{\rho}\frac{\partial p}{\partial x} - \frac{2(\zeta+2)\pi\mu}{\rho}\frac{Q}{A} \end{aligned} \tag{A.1}$$

Typically, the system is closed by some experimental or theoretical tube law [47,48], which is a constitutive relation for the material which makes up the luminal boundary, and boundary conditions (see below). Such a formulation does not account for sequestration flow or vessel leak. Here, we further assume that quantities are steady $\psi(x,t) \to \psi(x)$, that $A(x)$ is a known function of centre-line distance x, and that inlet ($x = 0$) boundary conditions on pressure and flow are specified

$$p(0) = p_0, \quad Q(0) = Q_0.$$

These assumptions eliminate the need for a tube law.

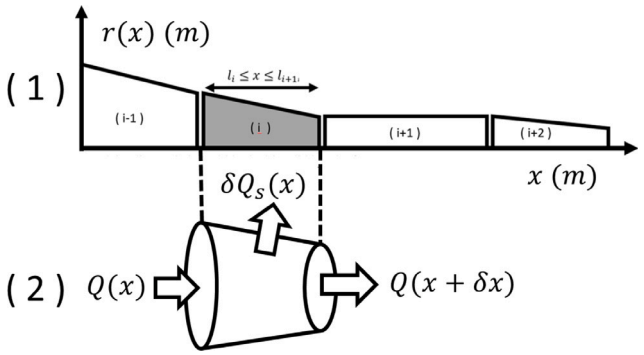

Fig. A.6. Schematic representation of the mathematical description of the artery. (1) A section of part of the artery, described by the function $r(x)$. Each element of the artery is assumed to be an axi-symmetric conical frustum. The ith element extends over the stream-wise co-ordinate interval $x_i \le x \le x_{i+1}$ (2) The ith element (shaded in (1)) shown in 3D, with the inlet, outlet and sequestration fluxes shown.

A.2. Anatomy description

We consider a set of six representative coronary arteries. All were clinically assessed as healthy. These were derived from stereoscopic coronary angiography, using epipolar geometry. In addition to artery geometry, patients' proximal inlet flow and (aortic) pressure were measured, using Rayflow™ catheterisation and a pressure wire. These geometries have been low-pass Fourier filtered, to remove minor stenoses, by ensuring radius is monotonically decaying function of stream-wise co-ordinate, x. (This was simply achieved by truncating a complex exponential Fourier series decomposition truncated at 6 terms). Proximal pressure and flow boundary conditions are those measured.

Let us first parameterise a 1D model of such and artery. Fig. A.6 shows schematic. All arteries treated in this work may be described as set-out here. We choose to represent each compartment of the artery as a truncated conic frustum. The ith segment, or *solid*, corresponds to $x : x_i \le x \le x_{i+1}$. Each solid is of course axi-symmetric. The luminal radius variation within the ith solid is described as follows

$$r(x) = r_i + m_i(x - x_i), \quad x_i \le x \le x_{i+1}, \quad i = 1, \ldots, N$$

The vessel is defined by a set of radius samples $\{(x_i, r_i), i = 1, \ldots, N\}$. In health, radius is a monotonically decaying function of vessel length

$$r_i \ge r_{i+1}, i = 1, \ldots, (N-1), \quad m_i < 0.$$

A.3. Anatomical leak description

We formulate a model of wall sequestration flux, or vessel leak based upon anatomy (i.e. the local taper of the artery) and Murray's law [16]. The value of Murray's law exponent is contested and we will denote its value by p, note. Recall, we consider the steady-state case, when artery flow Q, and area A depend solely on the distance along the artery, x.

The sequestration flux across the boundary of a length element of the artery, at position x, is denoted $\delta Q_s(x)$. See Fig. A.6. Therefore, the cumulative sequestration flux, over all length elements proximal to x is given by

$$Q_s(x) = \int_0^x dQ_s(u)du$$

Conservation of mass may now be expressed as follows

$$Q(x) + Q_s(x) = Q_0,$$

and differentiating with respect to x, it follows

$$\frac{dQ}{dx} = -\frac{dQ_s}{dx}.$$

Now, taper in any vessel section is taken to imply the existence of an unresolved branch vessel. We model the resolved, luminal, boundary as a right circular conical frustum with height δx and base location x. Applying Murray's law to this system, we have

$$Q(x+\delta x) = Q(x)\left(\frac{A(x+\delta x)}{A(x)}\right)^{\frac{c}{2}}$$

where c is the Murray exponent. Expanding about x, using first order binomial expansions and cancelling terms

$$\frac{dQ}{dx} = Q(x)\frac{c}{2}\frac{1}{A(x)}\frac{dA}{dx},$$

where all derivatives are evaluated at x. We note that the above is a continuity equation for a one-dimensional system in which there is sequestration. Separating variables and using properties of logarithms it is straightforward to show

$$\frac{d}{dx}\log(Q(x)) = \frac{d}{dx}\log(A(x))^{\frac{c}{2}}.$$

Integrate over $x \in [0, X < L]$ to yield $\log\left(\frac{Q(X)}{Q(0)}\right) = \log\left(\frac{A(X)}{A(0)}\right)^{\frac{c}{2}}$, then $X \to x$ to find the following algebraic relationship between $Q(x)$ and $A(x)$

$$Q(x) = Q(0)\left(\frac{A(x)}{A_0}\right)^{\frac{c}{2}}. \tag{A.2}$$

The corresponding cumulative sequestration flow up to the inlet of the ith conical frustum element is then

$$Q_s(x) = \left(1 - \left(\frac{A(x)}{A_0}\right)^{\frac{c}{2}}\right)Q(0). \tag{A.3}$$

We note that, for an anatomically-based leak model, both $Q(x)$ and $Q_s(x)$ are fully determined by the inlet flow and are independent of the 'history' of the vessel proximal to x. Further, $Q_s(x)$ is synonymous with vessel taper (where a vessel does not taper, flow is conserved and there is no sequestration).

A.4. No sequestration flow

The problem we seek numerically to solve for mono-variate functions $p(x)$, $q(x)$ is obtained by simplifying Eqs. (A.1), to produce a system of two coupled ODEs

$$\begin{aligned}\frac{dQ}{dx} &= 0 \\ \frac{d}{dx}\left(\frac{Q^2}{A}\right) &= -\frac{A}{\rho}\frac{dp}{dx} - \frac{2(\zeta+2)\pi\mu}{\rho}\frac{Q}{A}\end{aligned} \tag{A.4}$$

$$p(0) = p_0, \quad Q(0) = Q_0.$$

We proceed by eliminating variables. Integrate the first equation and fix flow to its inlet value $Q = Q_0$, a constant. Then, in the Navier–Stokes equation, perform the differentiation in left hand side and re-arrange

$$\frac{Q_0^2}{A^3}\frac{dA}{dx} = \frac{1}{\rho}\frac{dp}{dx} + \frac{2(\zeta+2)\pi\mu}{\rho}\frac{Q_0}{A^2}.$$

Integrating on x, over a range of stream-wise co-ordinate which corresponds to one conical frustum $x_i \le x \le x_{i+1}$

$$Q_0^2\left[\frac{A^{-2}}{-2}\right]_{x_i}^{x_{i+1}} = \frac{1}{\rho}[p]_{x_i}^{x_i+1} + \frac{2(\zeta+2)\pi\mu Q_0}{\rho}\int_{x_i}^{x_{i+1}} A^{-2}dx.$$

Processing the limits and making $p(x_{i+1})$ subject we straightforwardly obtain

$$p(x_{i+1}) = p(x_i) + \frac{\rho Q_0^2}{2A_i^2} - \frac{\rho Q_0^2}{2A_{i+1}^2} - 2(\zeta+2)\pi\mu Q_0\int_{x_i}^{x_{i+1}} A(x)^{-2}dx, \tag{A.5}$$

in agreement with Fossan et al. [21,26]. The integral might be evaluated using a suitable quadrature. The above result is further adapted in the next section.

A.5. Reference and modified anatomical models : anatomical sequestration flow

An approach to leak was validated by Gosling et al. [19], who devised a modified form of Eq. (A.5)

$$p(x_{i+1}) = p(x_i) + \frac{\rho Q_i^2}{2A_i^2} - \frac{\rho Q_{i+1}^2}{2A_{i+1}^2} - 2(\zeta+2)\pi\mu\int_{x_i}^{x_{i+1}} Q(x)A(x)^{-2}dx. \tag{A.6}$$

Gosling et al. account for leak by using the first of Eqs. (A.7) to determine Q_i and Q_{i+1}. Owing to its validated status, this approach to calculating pressure is taken as our gold standard, reference anatomical model.

When vessel flow is known (from Eq. (A.2)), the continuity equation (which now acquires an effective source, note) may be replaced in Eqs. (A.1) to yield a system of two differential algebraic equations for pressure and flow

$$\begin{aligned}Q &= Q_0\left(\frac{A}{A_0}\right)^{c/2} \\ \frac{d}{dx}\left(\frac{Q^2}{A}\right) &= -\frac{A}{\rho}\frac{dp}{dx} - \frac{2(\zeta+2)\pi\mu}{\rho}\frac{Q}{A}\end{aligned} \tag{A.7}$$

$$p(0) = p_0, \qquad Q(0) = Q_0.$$

We reserve for future work a consideration of the effect of the continuity source in the momentum equation, which, note, is not modified here. Eliminating Q and re-arranging we obtain the Navier–Stokes equation as follows

$$\frac{Q_0^2}{A_0^p}(c-1)A^{c-3}\frac{dA}{dx} = -\frac{1}{\rho}\frac{dp}{dx} - \frac{2(\zeta+2)\pi\mu}{\rho A_1^{\frac{c}{2}}}Q_0 A^{\frac{c}{2}-2}$$

Above c is the given Murrays exponent. Integrating on a range of x corresponding to one conical frustum, or solid, $x : x_i \le x \le x_{i+1}$, processing the limits and re-arranging

$$\begin{aligned}\frac{\rho Q_0^2}{A_0^c}\frac{(c-1)}{(c-2)}\left(A_{i+1}^{c-2} - A_i^{c-2}\right) &= -p(x_{i+1}) + p(x_i) \\ &\quad - \frac{2(\zeta+2)\pi\mu}{A_0^{\frac{c}{2}}}Q_0\int_{x_1}^{x_{i+1}} A^{\frac{c}{2}-2}dx\end{aligned} \tag{A.8}$$

Above, the left hand side represents inertia, the last term on the right hand side viscosity. Transposing the inertia and pressure terms

$$p(x_{i+1}) = p(x_i) + \frac{\rho Q_0^2}{A_0^p}\frac{(c-1)}{(c-2)}\left(A_i^{c-2} - A_{i+1}^{c-2}\right) - \frac{2(\zeta+2)\pi\mu}{A_0^{\frac{c}{2}}}Q_0\int_{x_1}^{x_{i+1}} A^{\frac{c}{2}-2}dx \tag{A.9}$$

In health $A_i \ge A_{i+1}$. Since all estimates place $c > 2.33$, the inertia term in the above is positive, as is the integral. Hence, the sign of the pressure drop is dictated by the balance between the inertia and viscous terms. For a negative pressure change (drop), viscous loss must dominate. To establish the most transparent correspondence with Gosling et al. [19], we take Eq. (A.9) and re-write the inertia terms. For the nth conic frustum $\frac{Q_0^2}{A_0^c}A_n^{c-2} = \frac{Q_0^2}{A_0^c}\frac{A_n^c}{A_n^2} = \left(Q_0^2\frac{A_n}{A_1}\right)^c\frac{1}{A_n^2} = \frac{Q_n^2}{A_n^2}, \quad \forall n.$

Now the Navier–Stokes equation's inertia terms can be re-cast. Making $p(x_{i+1})$ subject we obtain our modified anatomical model

$$\begin{aligned}p(x_{i+1}) &= p(x_i) + \rho\left(\frac{c-1}{c-2}\right)\frac{Q_i^2}{A_i^2} - \rho\left(\frac{c-1}{c-2}\right)\frac{Q_{i+1}^2}{A_{i+1}^2} \\ &\quad - \frac{2(\zeta+2)\pi\mu Q_0}{A_1^{\frac{c}{2}}}\int_{x_1}^{x_{i+1}} A^{\frac{c}{2}-2}dx\end{aligned} \tag{A.10}$$

A.6. Conductivity model : physiological leak

We derive a model of a radial sequestration flux, $Q_s(x)$, based upon an assumption that artery walls behave as porous layers. The sequestration flux (units of m s^{-1} i.e. volume per unit area of luminal surface, per unit time) is driven by the transmural pressure in accord with Darcy's law, blood viscosity and the porous layer effective permeability, $\alpha(x)$ [29]. For a conical frustum of height δx the increment in $Q_s(x)$ is, to first order

$$dQ_s(x) = -\frac{\alpha(x)\{2\pi r(x)dx\}}{\mu}\left(\frac{p(x)-p_0}{t}\right).$$

Here, p_0 is cavity pressure, the expression within the braces is the luminal vessel segment area between locations x and $x+dx$, t is the wall thickness (which is assumed constant) and $\alpha(x)$ is the porosity of the wall material. The sequestration flow will be positive in the direction of the surface normal vector. This description is of course best suited to smaller vessels, rather than large branch vessels, in which inertia plays a significant role. We write this as follows

$$\frac{dQ_s}{dx} = K(x)p(x), \quad K(x) = \frac{2\pi r(x)\alpha(x)}{\mu t}. \tag{A.11}$$

Aggregate function $K(x)$ combines both anatomical and physiological information. It is an effective hydraulic conductivity. To assign it in a manner consistent with the other models of sequestration, we assign turn to the anatomical leak model.

Consider a conical frustum with proximal (distal) area A $(Q + dA)$, then

$$dQ_s = Q(A+dA) - Q(A).$$

Recall, for the anatomical leak we have $Q(x) = Q_0\left(\frac{A(x)}{A_0}\right)^{\frac{c}{2}}$. Substituting this result, we find

$$\frac{dQ_s}{Q_0} = \left(\frac{A+dA}{A_0}\right)^{\frac{c}{2}} - \left(\frac{A}{A_0}\right)^{\frac{c}{2}}.$$

This is readily re-expressed as follows

$$\frac{dQ_s}{Q_0} = \frac{1}{A_0^{\frac{c}{2}}}\left\{A^{\frac{c}{2}}\left(1+\frac{dA}{A}\right) - A^{\frac{c}{2}}\right\}.$$

Taking a first order binomial expansion in the right hand side of the above, this is reduced to the following

$$dQ_s = \frac{cQ_0}{2}\left(\frac{A}{A_0}\right)^{\frac{c}{2}}\frac{dA}{A}$$

Accordingly $\frac{dQ_s}{dx} = \frac{cQ_0}{2}\left(\frac{A}{A_0}\right)^{\frac{c}{2}}\frac{1}{A}\frac{dA}{dx}$ and hence

$$\frac{dQ_s}{dx} = \frac{c}{2}\frac{d\log(A)}{dx}Q(x) \tag{A.12}$$

Comparing Eqs. (A.11) and (A.12) it is immediate that

$$K(x) = \frac{c}{2}\frac{d\log(A(x))}{dx}\frac{Q(x)}{p(x)} \tag{A.13}$$

Given our assumptions regarding the assignment of $K(x)$ from the physiological leak model, $K(x) > 0,\ \forall x$.

In summary, an effective hydraulic conductance for the artery wall material may be assigned by computing the pressure field and flow fields, using the Eqs. (A.5) and (A.2). The flow and pressure may then be used in Eq. (A.13) to assign the corresponding wall conductivity. Assigning $K(x)$ as described above, the result clearly reflects the side-branch structure of the vessel, for which taper is a surrogate. One therefore expects that in regions of larger taper (where one can infer a greater density of side-branches), leak should be greater and therefore conductance larger. The pressure and flow used to determine $K(x)$ were derived from our reference anatomical model.

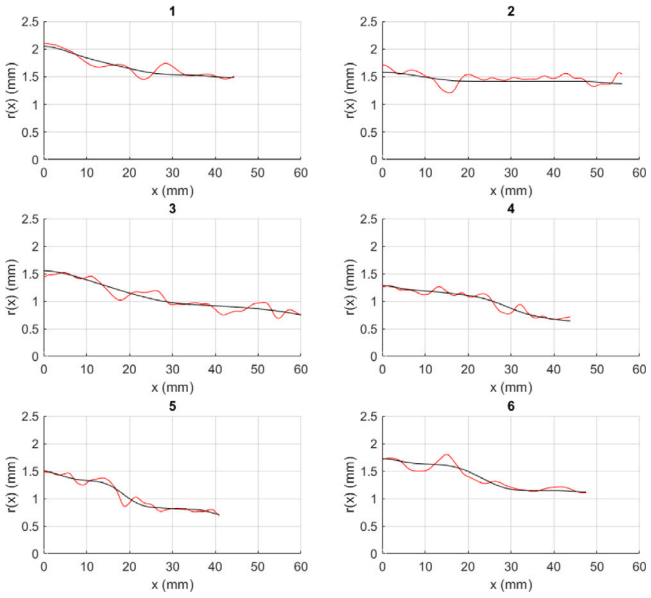

Fig. B.7. Patient geometries: The 6 idealised geometries used in this work with radius plotted against position in the artery. The red line represents the true artery, the black line is the Fourier filtered line.

A.6.1. Mathematical formulation

The problem of physiological leak is formulated as a coupled ODE problem, for $p(x)$ and $Q(x)$. Consider mass conservation in the form $Q(x) + Q_s(x) = Q_0$ (recall, $Q_s(x)$ is the cumulative sequestration flux). Differentiating on x and using Eq. (A.11), it is immediate that mass conservation may be expressed with a source as follows $\frac{dQ}{dx} = -K(x)p(x)$. A coupled ODE description of physiological leak, for a given wall hydraulic conductance function $K(x)$, may now be formulated as the following pair of non-linear ODEs

$$\begin{aligned}\frac{dQ}{dx} &= -K(x)p(x) \\ \frac{d}{dx}\left(\frac{Q^2}{A}\right) &= -\frac{A}{\rho}\frac{dp}{dx} - \frac{2(\zeta+2)\pi\mu}{\rho}\frac{Q}{A}\end{aligned} \tag{A.14}$$

Above we have again not modified the momentum equation for the presence of a continuity source. Expanding the left hand side of the momentum equation, and making the pressure derivative subject, we can straightforwardly re-arrange the system into the canonical state space system form

$$\begin{aligned}\frac{dQ}{dx} &= -K(x)p(x) \\ \frac{dp}{dx} &= \frac{\rho}{A^3}\frac{dA}{dx}Q^2 - \frac{2\rho}{A^2}\frac{dQ}{dx}Q - \frac{2(\zeta+2)\pi\mu}{A^2}Q\end{aligned} \tag{A.15}$$

Finally, eliminating the $\frac{dQ}{dx}$ in the second equation, in favour of the pressure, using the first, we have the following formulation

$$\begin{aligned}\frac{dQ}{dx} &= -\frac{K(x)}{\delta x}p(x) \\ \frac{dp}{dx} &= \frac{\rho}{A^3}\frac{dA}{dx}Q^2 + \frac{2\rho K(x)}{A^2}Qp(x) - \frac{2(\zeta+2)\pi\mu}{A^2}Q\end{aligned} \tag{A.16}$$

The formulation above solved using and explicit Runge–Kutta algorithm, with an effective hydraulic conductance in accord with the vessel geometry, using Eq. (A.13).

Appendix B. Patient specific geometries

See Fig. B.7.

References

[1] F.-J. Neumann, M. Sousa-Uva, A. Ahlsson, F. Alfonso, A.P. Banning, U. Benedetto, R.A. Byrne, J.-P. Collet, V. Falk, S.J. Head, et al., 2018 ESC/EACTS guidelines on myocardial revascularization, Eur. Heart J. 40 (2) (2019) 87–165, http://dx.doi.org/10.1093/eurheartj/ehy394.

[2] P.A. Tonino, B. De Bruyne, N.H. Pijls, U. Siebert, F. Ikeno, M. vant Veer, V. Klauss, G. Manoharan, T. Engstrøm, K.G. Oldroyd, et al., Fractional flow reserve versus angiography for guiding percutaneous coronary intervention, N. Engl. J. Med. 360 (3) (2009) 213–224, http://dx.doi.org/10.1056/NEJMoa0807611.

[3] M. Vecsey-Nagy, B. Szilveszter, M. Kolossvary, M. Boussoussou, B. Vattay, X. Gonda, Z. Rihmer, B. Merkely, P. Maurovich-Horvat, J. Nemcsik, Association between affective temperaments and severe coronary artery disease, J. Affect. Disord. 295 (2021) 914–919.

[4] T.G. Scully, L. Toner, J. Yeoh, O. Farouque, M.B. Yudi, M. Horrigan, D.J. Clark, Safety and long-term clinical outcomes of fractional flow reserve guided coronary revascularisation, Heart Lung Circ. 30 (9) (2021) 1343–1347.

[5] C.A. Taylor, T.A. Fonte, J.K. Min, Computational fluid dynamics applied to cardiac computed tomography for noninvasive quantification of fractional flow reserve: scientific basis, J. Am. Coll. Cardiol. 61 (22) (2013) 2233–2241.

[6] P.D. Morris, D. Ryan, A.C. Morton, R. Lycett, P.V. Lawford, D.R. Hose, J.P. Gunn, Virtual fractional flow reserve from coronary angiography: modeling the significance of coronary lesions: results from the VIRTU-1 (virtual fractional flow reserve from coronary angiography) study, JACC: Cardiovasc. Interv. 6 (2) (2013) 149–157.

[7] M. Ghobrial, H.A. Haley, R. Gosling, V. Rammohan, P.V. Lawford, D.R. Hose, J.P. Gunn, P.D. Morris, The new role of diagnostic angiography in coronary physiological assessment, Heart 107 (10) (2021) 783–789.

[8] M. Vardhan, J. Gounley, S.J. Chen, A.M. Kahn, J.A. Leopold, A. Randles, The importance of side branches in modeling 3D hemodynamics from angiograms for patients with coronary artery disease, Sci. Rep. 9 (1) (2019) 1–10.

[9] M.L. Rizzini, A. Candreva, C. Chiastra, E. Gallinoro, K. Calò, F. D'Ascenzo, B. De Bruyne, T. Mizukami, C. Collet, D. Gallo, et al., Modelling coronary flows: impact of differently measured inflow boundary conditions on vessel-specific computational hemodynamic profiles, Comput. Methods Programs Biomed. 221 (2022) 106882.

[10] E. Wellnhofer, J. Osman, U. Kertzscher, K. Affeld, E. Fleck, L. Goubergrits, Flow simulation studies in coronary arteries—impact of side-branches, Atherosclerosis 213 (2) (2010) 475–481.

[11] J.T. Schrauwen, J.C. Schwarz, J.J. Wentzel, A.F. van der Steen, M. Siebes, F.J. Gijsen, The impact of scaled boundary conditions on wall shear stress computations in atherosclerotic human coronary bifurcations, Am. J. Physiol. Heart Circ. Physiol. 310 (10) (2016) H1304–H1312.

[12] W. Li, K. Lian, Y. Chen, S. Zhao, X. Guo, Q. Tao, H. Gao, S. Xie, C. Li, Q. Wang, et al., Computing intracoronary blood flow rate under incomplete boundary conditions: Combing coronary anatomy and fractional flow reserve, Med. Eng. Phys. 111 (2023) 103942.

[13] S. Tu, E. Barbato, Z. Köszegi, J. Yang, Z. Sun, N.R. Holm, B. Tar, Y. Li, D. Rusinaru, W. Wijns, et al., Fractional flow reserve calculation from 3-dimensional quantitative coronary angiography and TIMI frame count: a fast computer model to quantify the functional significance of moderately obstructed coronary arteries, JACC: Cardiovasc. Interv. 7 (7) (2014) 768–777.

[14] P.T. Gamage, P. Dong, J. Lee, Y. Gharaibeh, V.N. Zimin, H.G. Bezerra, D.L. Wilson, L. Gu, Fractional flow reserve (FFR) estimation from OCT-based CFD simulations: Role of side branches, Appl. Sci. 12 (11) (2022) 5573.

[15] P.D. Morris, R. Gosling, I. Zwierzak, H. Evans, L. Aubiniere-Robb, K. Czechowicz, P.C. Evans, D.R. Hose, P.V. Lawford, A.J. Narracott, et al., A novel method for measuring absolute coronary blood flow and microvascular resistance in patients with ischaemic heart disease, Cardiovasc. Res. 117 (6) (2021) 1567–1577.

[16] C.D. Murray, The physiological principle of minimum work: I. The vascular system and the cost of blood volume, Proc. Natl. Acad. Sci. 12 (3) (1926) 207–214.

[17] Y. Huo, G.S. Kassab, A scaling law of vascular volume, Biophys. J. 96 (2) (2009) 347–353.

[18] A. Kamiya, T. Togawa, Optimal branching structure of the vascular tree, Bull. Math. Biophys. 34 (1972) 431–438.

[19] R.C. Gosling, J. Sturdy, P.D. Morris, F.E. Fossan, L.R. Hellevik, P. Lawford, D.R. Hose, J. Gunn, Effect of side branch flow upon physiological indices in coronary artery disease, J. Biomech. 103 (2020) 109698.

[20] D.J. Taylor, J. Feher, K. Czechowicz, I. Halliday, D. Hose, R. Gosling, L. Aubiniere-Robb, M. van't Veer, D.C. Keulards, P. Tonino, et al., Validation of a novel numerical model to predict regionalized blood flow in the coronary arteries, Eur. Heart J. Digit. Health 4 (2) (2023) 81–89.

[21] F.E. Fossan, J. Sturdy, L.O. Müller, A. Strand, A.T. Bråten, A. Jø rgensen, R. Wiseth, L.R. Hellevik, Uncertainty quantification and sensitivity analysis for computational FFR estimation in stable coronary artery disease, Cardiovasc. Eng. Technol. 9 (2018) 597–622.

[22] L. Aubiniere-Robb, R. Gosling, D.J. Taylor, T. Newman, D.R. Hose, I. Halliday, P.V. Lawford, A.J. Narracott, J.P. Gunn, P.D. Morris, The complementary value of absolute coronary flow in the assessment of patients with ischaemic heart disease, Nature Cardiovasc. Res. 1 (7) (2022) 611–616.

[23] M. van't Veer, J. Adjedj, I. Wijnbergen, G.G. Toth, M. Rutten, E. Barbato, L.X. van Nunen, N. Pijls, B. De Bruyne, Novel monorail infusion catheter for volumetric coronary blood flow measurement in humans: in vitro validation, EuroIntervention 12 (6) (2016) 701–707.

[24] F. Gijsen, Y. Katagiri, P. Barlis, C. Bourantas, C. Collet, U. Coskun, J. Daemen, J. Dijkstra, E. Edelman, P. Evans, et al., Expert recommendations on the assessment of wall shear stress in human coronary arteries: existing methodologies, technical considerations, and clinical applications, Eur. Heart J. 40 (41) (2019) 3421–3433.

[25] W. Aarnoudse, M. van't Veer, N.H. Pijls, J. Ter Woorst, S. Vercauteren, P. Tonino, M. Geven, M. Rutten, E. van Hagen, B. de Bruyne, et al., Direct volumetric blood flow measurement in coronary arteries by thermodilution, J. Am. Coll. Cardiol. 50 (24) (2007) 2294–2304.

[26] F.E. Fossan, Physics-Based and Data-Driven Reduced Order Models: Applications to Coronary Artery Disease Diagnostics (Ph.D. thesis), NTNU, 2020.

[27] F. Liang, K. Fukasaku, H. Liu, S. Takagi, A computational model study of the influence of the anatomy of the circle of willis on cerebral hyperperfusion following carotid artery surgery, Biomed. Eng. Online 10 (2011) 1–22.

[28] L.F. Shampine, M.W. Reichelt, The matlab ode suite, SIAM J. Sci. Comput. 18 (1) (1997) 1–22.

[29] S. Whitaker, Flow in porous media I: A theoretical derivation of Darcy's law, Transp. Porous Media 1 (1986) 3–25.

[30] D.F. Young, F.Y. Tsai, Flow characteristics in models of arterial stenoses—I. Steady flow, J. Biomech. 6 (4) (1973) 395–410.

[31] D.F. Young, F.Y. Tsai, Flow characteristics in models of arterial stenoses—II. Unsteady flow, J. Biomech. 6 (5) (1973) 547–559.

[32] F.E. Fossan, L.O. Müller, J. Sturdy, A.T. Bråten, A. Jø rgensen, R. Wiseth, L.R. Hellevik, Machine learning augmented reduced-order models for FFR-prediction, Comput. Methods Appl. Mech. Engrg. 384 (2021) 113892.

[33] N.H. Pijls, B. Van Gelder, P. Van der Voort, K. Peels, F.A. Bracke, H.J. Bonnier, M.I. El Gamal, Fractional flow reserve: a useful index to evaluate the influence of an epicardial coronary stenosis on myocardial blood flow, Circulation 92 (11) (1995) 3183–3193.

[34] P. Xaplanteris, S. Fournier, N.H. Pijls, W.F. Fearon, E. Barbato, P.A. Tonino, T. Engstrøm, S. Kääb, J.-H. Dambrink, G. Rioufol, et al., Five-year outcomes with PCI guided by fractional flow reserve, N. Engl. J. Med. 379 (3) (2018) 250–259.

[35] R.V. Parikh, G. Liu, M.E. Plomondon, T.S. Sehested, M.A. Hlatky, S.W. Waldo, W.F. Fearon, Utilization and outcomes of measuring fractional flow reserve in patients with stable ischemic heart disease, J. Am. Coll. Cardiol. 75 (4) (2020) 409–419.

[36] J. Knuuti, W. Wijns, A. Saraste, D. Capodanno, E. Barbato, C. Funck-Brentano, E. Prescott, R.F. Storey, C. Deaton, T. Cuisset, et al., 2019 ESC guidelines for the diagnosis and management of chronic coronary syndromes: the task force for the diagnosis and management of chronic coronary syndromes of the European society of cardiology (ESC), Eur. Heart J. 41 (3) (2020) 407–477.

[37] E. Amsterdam, J. Boyd, M.R.P. Bullock-Palmer, F.T. Conejo, D.B. Diercks, F.-F. Gentile, J.P. Greenwood, F. FSCMR, D.A. Morrow, F.R.E. O'Connor, et al., 2021 AHA/ACC/ASE/CHEST/SAEM/SCCT/SCMR guideline for the evaluation and diagnosis of chest pain, J. Am. Coll. Cardiol. 78 (22) (2021).

[38] O.M. Demir, C.K. Boerhout, G.A. de Waard, T.P. van de Hoef, N. Patel, M.A. Beijk, R. Williams, H. Rahman, H. Everaars, R.K. Kharbanda, et al., Comparison of Doppler flow velocity and thermodilution derived indexes of coronary physiology, Cardiovasc. Interv. 15 (10) (2022) 1060–1070.

[39] D.J. Taylor, L. Aubiniere-Robb, R. Gosling, T. Newman, D.R. Hose, I. Halliday, P.V. Lawford, A.J. Narracott, J.P. Gunn, P.D. Morris, Sex differences in coronary microvascular resistance measured by a computational fluid dynamics model, Front. Cardiovasc. Med. 10 (2023).

[40] D.J. Taylor, J. Feher, I. Halliday, D.R. Hose, R. Gosling, L. Aubiniere-Robb, M. van't Veer, D. Keulards, P.A. Tonino, M. Rochette, et al., Refining our understanding of the flow through coronary artery branches; revisiting Murray's law in human epicardial coronary arteries, Front. Physiol. 13 (2022) 527.

[41] P.J. Blanco, G.H.V. Dos Santos, C.A. Bulant, A.M. Alvarez, F.A. Oliveira, G. Cunha-Lima, P.A. Lemos, Scaling laws and the left main coronary artery bifurcation. A combination of geometric and simulation analyses, Med. Eng. Phys. 99 (2022) 103701.

[42] M.A. Changizi, C. Cherniak, Modeling the large-scale geometry of human coronary arteries, Can. J. Physiol. Pharmacol. 78 (8) (2000) 603–611.

[43] N.R. Smilowitz, O. Toleva, A. Chieffo, D. Perera, C. Berry, Coronary microvascular disease in contemporary clinical practice, Circ.: Cardiovasc. Interv. (2023) e012568.

[44] W. Huberts, S.G. Heinen, N. Zonnebeld, D.A. van den Heuvel, J.-P.P. de Vries, J.H. Tordoir, D.R. Hose, T. Delhaas, F.N. van de Vosse, What is needed to make cardiovascular models suitable for clinical decision support? A viewpoint paper, J. Comput. Sci. 24 (2018) 68–84.

[45] D.R. Hose, P.V. Lawford, W. Huberts, L.R. Hellevik, S.W. Omholt, F.N. van de Vosse, Cardiovascular models for personalised medicine: Where now and where next? Med. Eng. Phys. 72 (2019) 38–48.

[46] T.J. Hughes, J. Lubliner, On the one-dimensional theory of blood flow in the larger vessels, Math. Biosci. 18 (1–2) (1973) 161–170.

[47] R.J. Whittaker, M. Heil, O.E. Jensen, S.L. Waters, A rational derivation of a tube law from shell theory, Q. J. Mech. Appl. Math. 63 (4) (2010) 465–496.

[48] F.E. Fossan, Comparison of Numerical Schemes for Nonlinear 1-D Arterial Blood Flow Modeling (Master's thesis), NTNU, 2015.